ACS APPLIED MATERIALS & INTERFACES

Research Article

Cite This: ACS Appl. Mater. Interfaces 2018, 10, 11699−11707

www.acsami.org

Copper-Substituted Lead Perovskite Materials Constructed with Different Halides for Working $(CH_3NH_3)_2CuX_4$-Based Perovskite Solar Cells from Experimental and Theoretical View

Ahmed Mourtada Elseman,*[,†,‡,∥] Ahmed Esmail Shalan,*[,†,∥] Sajid Sajid,[‡] Mohamed Mohamed Rashad,[†] Ali Mostafa Hassan,[§] and Meicheng Li[‡]

[†]Electronic & Magnetic Materials Department, Advanced Materials Division, Central Metallurgical Research and Development Institute (CMRDI), Helwan, P.O. Box 87, Cairo 11421, Egypt

[‡]State Key Laboratory of Alternate Electrical Power, System with Renewable Energy Sources, School of Renewable Energy, North China Electric Power University, Beijing 102206, China

[§]Chemistry Department, Faculty of Science, Al-Azhar University, P.O. Box 11884, Nasr city, Cairo 11421, Egypt

Supporting Information

ABSTRACT: Toxicity and chemical instability issues of halide perovskites based on organic−inorganic lead-containing materials still remain as the main drawbacks for perovskite solar cells (PSCs). Herein, we discuss the preparation of copper (Cu)-based hybrid materials, where we replace lead (Pb) with nontoxic Cu metal for lead-free PSCs, and investigate their potential toward solar cell applications based on experimental and theoretical studies. The formation of $(CH_3NH_3)_2CuX_4$ [$(CH_3NH_3)_2CuCl_4$, $(CH_3NH_3)_2CuCl_2I_2$, and $(CH_3NH_3)_2CuCl_2Br_2$] was discussed in details. Furthermore, it was found that chlorine (Cl^-) in the structure is critical for the stabilization of the formed compounds. Cu-based perovskite-like materials showed attractive absorbance features extended to the near-infrared range, with appropriate band gaps. Green photoluminescence of these materials was obtained because of Cu^+ ions. The power conversion efficiency was measured experimentally and estimated theoretically for different architectures of solar cell devices.

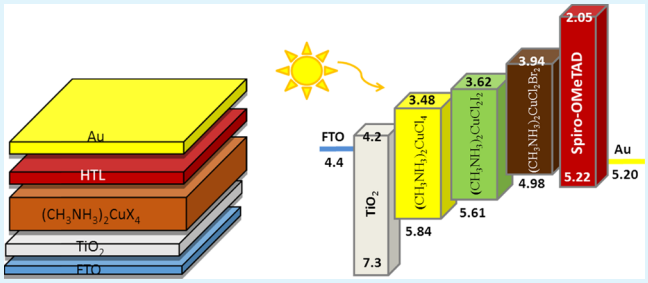

KEYWORDS: *lead-free, copper, halides, perovskite solar cells, optical properties*

INTRODUCTION

Miyasaka and co-workers in 2009 were the pioneers to use organometallic perovskites, and an efficiency of 3.8% was achieved for the solar cells assembled.[1] After that, a breakthrough occurred for improvement of record conversion efficiencies of organic−inorganic halide perovskite solar cells (PSCs) over 22%.[2,3] The generic structure of ABX_3 for hybrid organic−inorganic halide perovskite materials has attracted a formidable interest in this kind of cell community.[4−9] On one hand, these materials exhibit many advantages because of their long-range electron and hole diffusion lengths and suitable band gaps for assembling solar cells and can be easily attained into thin films through a low-temperature solution-based process.[10,11] On the other hand, despite their high power conversion efficiency (PCE), the high toxicity and chemical instability of the lead (Pb) in perovskite materials limit their commercialization and consider to be major disadvantages of $APbX_3$ perovskite materials. These challenges force the researchers to develop Pb-free perovskite devices while maintaining the high performance and good stability. Group 14 elements such as Sn and Ge are the most practicable metals to replace Pb in $MAPbI_3$ perovskite structures.[12,13] Some other elements such as Sb and Bi were also considered as an effective surrogate for Pb in the perovskite structure.[14−16] The reason behind the large PCE differences compared with the normal lead perovskite materials is the high air sensitivity of other metals such as Sn^{2+}, which is easily oxidized into Sn^{4+}. This problem may degrade the reproducibility and durability of these devices. To overcome the poor performance problem of these materials, a rigid processing environment and an encapsulation technique should be incorporated. Nowadays, replacing the toxic lead in perovskite structures with alternative cost-effective materials, environmentally friendly, less-toxic, and earth-abundant elements such as transition metals is an important target for improving PSCs. One can mention the interest which the transition metals (e.g., Fe^{2+}, Cu^{2+}, and Zn^{2+}) obtained to replace the toxic lead metals in clean PSCs. Indeed, replacing Pb with Cu has been a novel development for PSCs.

Received: January 10, 2018
Accepted: March 16, 2018
Published: March 16, 2018

DOI: 10.1021/acsami.8b00495
ACS Appl. Mater. Interfaces 2018, 10, 11699−11707

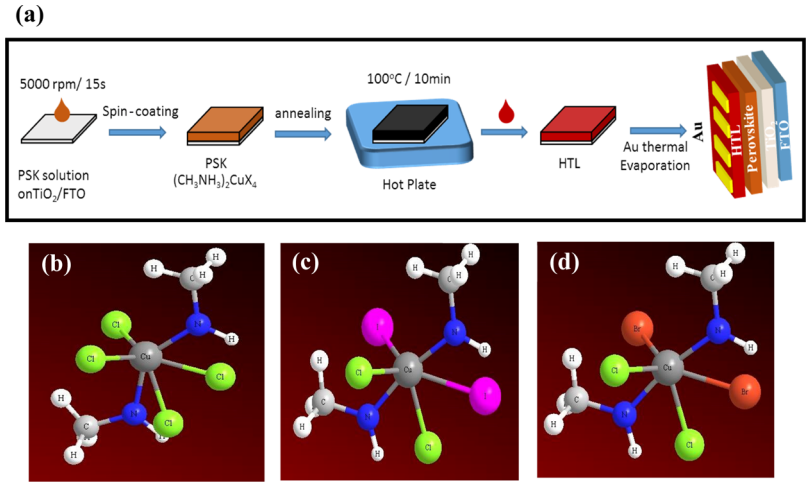

Figure 1. (a) Schematic diagram of the preparation of our lead-free PSC and (b–d) molecular modeling and chemicals structures of $(CH_3NH_3)_2CuCl_4$, $(CH_3NH_3)_2CuCl_2I_2$, and $(CH_3NH_3)_2CuCl_2Br_2$ powders, respectively.

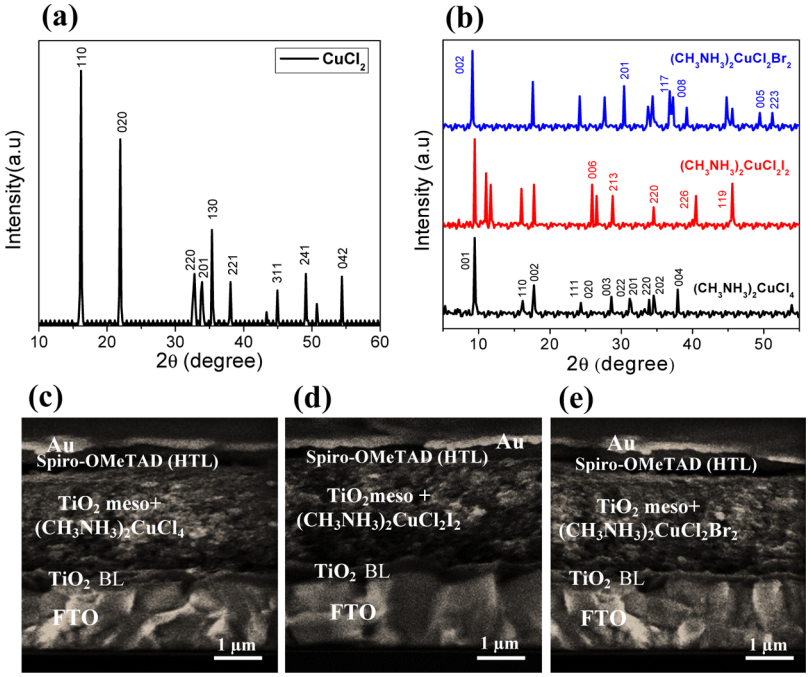

Figure 2. (a) XRD patterns of $CuCl_2$, (b) XRD of $(CH_3NH_3)_2CuCl_4$, $(CH_3NH_3)_2CuCl_2I_2$, and $(CH_3NH_3)_2CuCl_2Br_2$ powders, and (c–e) cross-sectional SEM images of the solar cells with the configuration of glass/FTO/TiO_2/$(CH_3NH_3)_2CuX$ (X = Cl_4, Cl_2I_2, and Cl_2Br_2 materials) perovskite/spiro-OMeTAD (HTL)/Au.

In this paper, green copper (Cu)-based hybrid perovskite materials with the general formula of $(CH_3NH_3)_2CuX$ (X = Cl_4, Cl_2I_2, and Cl_2Br_2) have been synthesized, characterized, and investigated for environment-friendly PSCs. We study copper metal as a suitable alternative element to change lead in metal halide perovskites and the functionality from experimental and theoretical view. The results show that copper reduction decreased and the material stability as well as the perovskite crystallization enhanced with the existence of Cl^- halide ions.[17] In addition, tuning of the optical absorption within the wavelength (λ = 300–900 nm) range, that is, visible to near-infrared range, can be achieved by changing the Cl/I/Br content ratio. To the best of our knowledge, only one published paper concerned about using lead-free perovskites based on copper as a transition metal for perovskite materials in photovoltaic applications.[17] This approach motivates us to find a solution for improving the material features as well as solar cell performance by replacing Pb by Cu-based perovskites and also to fill the gap with the state-of-the-art Pb-based perovskite devices.

RESULTS AND DISCUSSION

$(CH_3NH_3)_2CuCl_4$ as well as $(CH_3NH_3)_2CuCl_2X_2$ (X = I and Br) have been prepared through a grinding milling pathway. The mixed halide perovskite composition can be varied by changing the precursor halide ($CuCl_2$ with CH_3NH_3X, where X = Cl^-, I^-, and Br^-). The microstructure, particle size, crystal structure, and electrical and optical properties of $(CH_3NH_3)_2CuCl_4$, $(CH_3NH_3)_2CuCl_2I_2$, and $(CH_3NH_3)_2CuCl_2Br_2$ with the effect of halide ion substitutions

DOI: 10.1021/acsami.8b00495
ACS Appl. Mater. Interfaces 2018, 10, 11699–11707

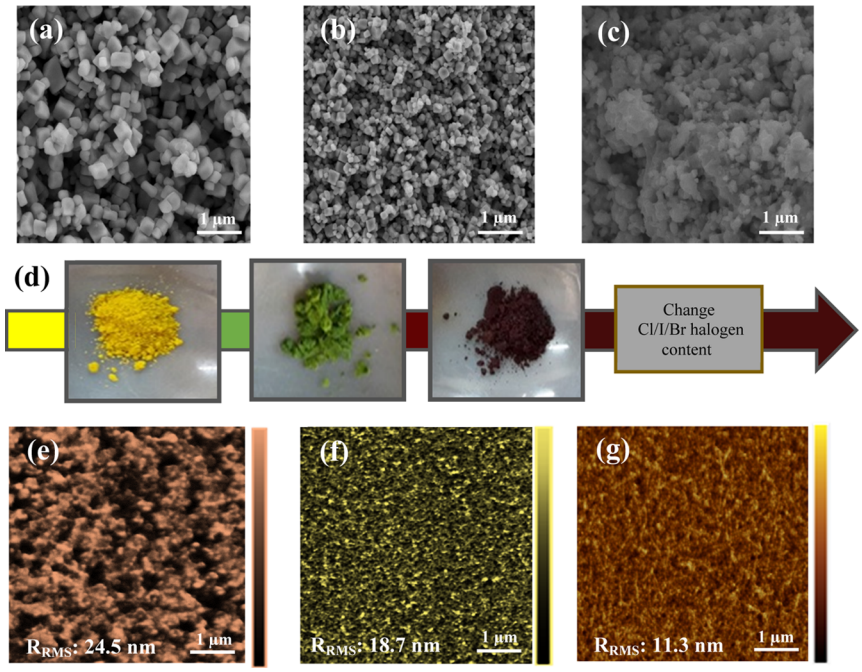

Figure 3. (a–c) FE-SEM micrographs; (d) photographs showing the color shift of the material powders with the change of the Cl/I/Br halogen content: $(CH_3NH_3)_2CuCl_4$ (yellow), $(CH_3NH_3)_2CuCl_2I_2$ (green), and $(CH_3NH_3)_2CuCl_2Br_2$ (dark brown); and (e–g) AFM images of the as-prepared materials by the milling method for $(CH_3NH_3)_2CuCl_4$, $(CH_3NH_3)_2CuCl_2I_2$, and $(CH_3NH_3)_2CuCl_2Br_2$, respectively.

were distinguished by X-ray diffraction (XRD), UV–vis spectroscopy, and field emission scanning electron microscopy (FE-SEM) techniques. Figure 1a illustrates a schematic diagram of the preparation to fabricate our $(CH_3NH_3)_2CuX_4$ device step by step; the details are discussed in the Experimental Methods. Furthermore, Figure 1b–d shows the molecular modeling and drawings of the chemical structures for $(CH_3NH_3)_2CuCl_4$, $(CH_3NH_3)_2CuCl_2I_2$, and $(CH_3NH_3)_2CuCl_2Br_2$. They give us the theories of chemical reaction observation through HyperChem series of programs. Herein, the molecular structures of $(CH_3NH_3)_2CuCl_4$, $(CH_3NH_3)_2CuCl_2I_2$, and $(CH_3NH_3)_2CuCl_2Br_2$ compounds were calculated through semiempirical PM3 and AM1 methods. Table S1 (Supporting Information) demonstrates the geometric structures that used as a base in calculating different parameters like total energy, binding energy, isolated atomic energy, and electronic energy, heat of formation, dipole moment, highest occupied molecular orbital (HOMO) and lowest unoccupied molecular orbital (LUMO) for the components used in this study.[18] The values obtained confirm the ability of copper-based perovskite compounds to be used as promising light absorber materials for photovoltaic applications.

Additionally, XRD patterns were used to confirm the synthetic $CuCl_2$ powder structure before using in the experiments, as illustrated in Figure 2a. Diffraction peaks at 2θ of 16.16°, 21.92°, 32.8°, 33.92°, 35.36°, 38.08°, 44.96°, 49.12°, and 54.4° assigned to the (110), (020), (220), (201), (130), (221), (311), (241), and (042) planes, respectively, of orthorhombic copper chloride (JCPDS 21-0297) were observed.[19,20] In addition, Figure 2b illustrates the XRD patterns of the organocopper halide perovskite structures $(CH_3NH_3)_2CuCl_4$, $(CH_3NH_3)_2CuCl_2I_2$, and $(CH_3NH_3)_2CuCl_2Br_2$. The composition of CH_3NH_3X (X = Cl, I, and Br) materials was previously detected by their XRD profile after their synthesis.[21] The crystallinity structure of the prepared compound powders was confirmed to be good by XRD spectra before any further characterization of organometal halide materials. Plainly, the results indicated that $(CH_3NH_3)_2CuCl_4$ is monoclinic, whereas the other materials with mixed halides $(CH_3NH_3)_2CuCl_2I_2$ and $(CH_3NH_3)_2CuCl_2Br_2$ were crystallized with an orthorhombic crystal shape. Substitution of Cl^- with I^- or Br^- has different effects on bond angles and unit cell dimension as well as ionic radius.[36] Experientially, the optimal stability range of the 3D perovskite structure was found to be in the window of $0.8 < t < 0.9$ and $0.442 < \mu < 0.895$, with a major formula of $(CH_3NH_3)_2CuX_4$.[22] Assuming the ionic radius of methyl ammonium R_{MA} = 180 pm,[22] the hypothetical perovskite $(CH_3NH_3)_2CuCl_4$ will have $t = 1.004$ and $\mu = 0.403$, clearly out of the stability range, and the rearrangement into a perovskite with lower dimensionality can be prophesied easily.[17] The cells constructed layer by layer can be affirmed by characterizing the cross sections with an FE-SEM technique. Figure 2c–e confirms the cross section of a full cell for $(CH_3NH_3)_2CuCl_4$, $(CH_3NH_3)_2CuCl_2I_2$, and $(CH_3NH_3)_2CuCl_2Br_2$ perovskite materials. A thin-film layer of TiO_2 as a compact layer was coated on fluorine-doped tin oxide (FTO) for all cells. Subsequently, a mesoporous TiO_2 layer was spin-coated, followed by a film of $(CH_3NH_3)_2CuX_4$ perovskite materials. An organic hole transport layer (HTL) (spiro-OMeTAD) was spin-coated on top of the PSK layer. Finally, a gold contact electrode with a thickness of approximately 100 nm was thermally evaporated on the top of the assembled cells. Appropriate connection between each layer was confirmed with the cross-sectional images, which expedites charge migration, which enhances the conversion efficiency of the assembled cells, as shown below in the results. The large surface area and good morphology obtained through the blocking and mesoporous TiO_2 layers show an essential effect for interfacial charge extraction. This can enhance the charge extraction and inhibit direct contact of the hole with the FTO substrate.

DOI: 10.1021/acsami.8b00495
ACS Appl. Mater. Interfaces 2018, 10, 11699–11707

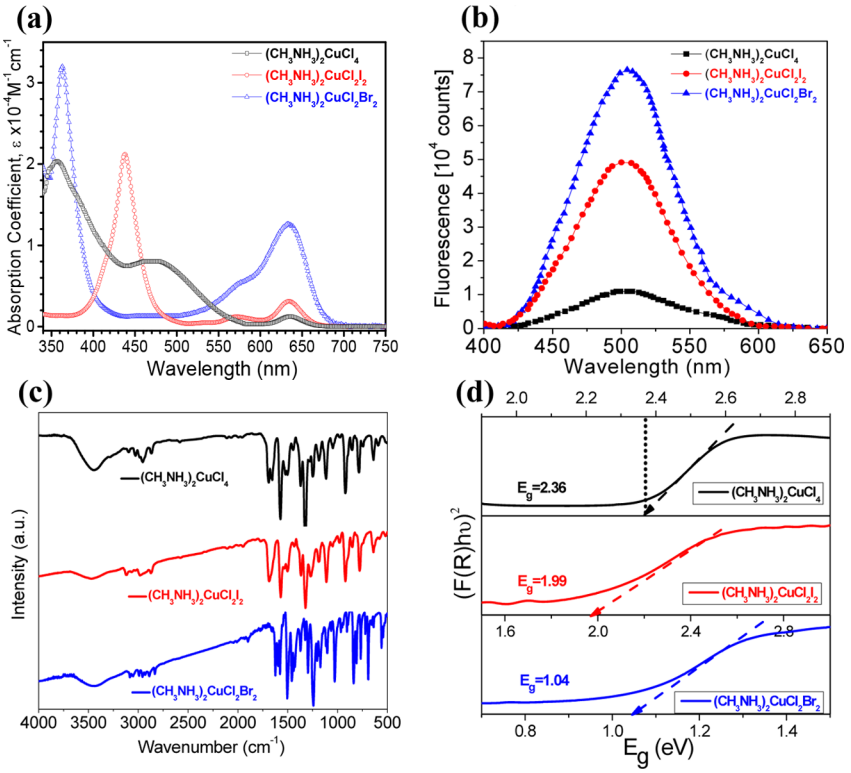

Figure 4. (a) Absorption coefficient, (b) PL spectra, (c) FT-IR spectral data, and (d) optical band gap energy for perovskites of the $(CH_3NH_3)_2CuCl_4$, $(CH_3NH_3)_2CuCl_2I_2$, and $(CH_3NH_3)_2CuCl_2Br_2$ materials synthesized by the grinding method.

Figure 3a–c evinces the morphology of each organocopper halide perovskite powder using FE-SEM micrographs. $(CH_3NH_3)_2CuCl_4$ and $(CH_3NH_3)_2CuCl_2I_2$ powders (Figure 3a,b) displayed a cubelike well-distributed morphology. However, Figure 3c depicts the structures for $(CH_3NH_3)_2CuCl_2Br_2$, which were agglomerated, with some particles appeared as cubes. In addition, films of the obtained powders on the TiO_2 layer have been prepared and checked for more information to determine the homogeneity and crystallinity of these materials. The images of the obtained results are shown in Figure S1a–c, Supporting Information. In fact, the homogeneity of the films may affect the net efficiency of the cells. From Figure S1a, we can notice that the homogeneity of the obtained film for $(CH_3NH_3)_2CuCl_4$ is better than those of the other films obtained for $(CH_3NH_3)_2CuCl_2I_2$ and $(CH_3NH_3)_2CuCl_2Br_2$, as illustrated in Figure S1b,c, which can explain the reason behind the difference in the net conversion efficiency, which will be discussed later below. Besides, Figure 3d evidences the photographs of the as-prepared powders by the milling method obtained for $(CH_3NH_3)_2CuCl_4$, $(CH_3NH_3)_2CuCl_2I_2$, and $(CH_3NH_3)_2CuCl_2Br_2$. It can be seen that the color was progressively varied from yellow passing to green and finally appeared as brown for $(CH_3NH_3)_2CuCl_4$, $(CH_3NH_3)_2CuCl_2I_2$, and $(CH_3NH_3)_2CuCl_2Br_2$, respectively. This is due to the replacement of one ion of the three chloride ions by iodide and bromide. Furthermore, the corresponding atomic force microscopy (AFM) surface topographies of the same samples were investigated to recognize the leverage of the surface coverage of the different perovskite materials on the net efficiency obtained, as shown in Figure 3e,g. In contrast, the result indicates that the root-mean-square roughness (R_{rms}) values for $(CH_3NH_3)_2CuCl_2I_2$ and $(CH_3NH_3)_2CuCl_2Br_2$ films are significantly smaller than that of the $(CH_3NH_3)_2CuCl_4$ film. Additionally, R_{rms} of $(CH_3NH_3)_2CuCl_4$ was 24.5 nm, whereas they were 18.7 and 11.3 nm for $(CH_3NH_3)_2CuCl_2I_2$ and $(CH_3NH_3)_2CuCl_2Br_2$, respectively. The roughness of perovskite materials is a critical factor estimated to achieve a high-efficiency performance of a device.[23] A larger roughness of the $(CH_3NH_3)_2CuCl_4$ layer thus confirms that the surface coverage of this film is greater than those of the others, which would result in an enhancement in the efficiency of the cells based on the $(CH_3NH_3)_2CuCl_4$ film compared to those of the other perovskite films.[24]

The series of $(CH_3NH_3)_2CuCl_4$, $(CH_3NH_3)_2CuCl_2I_2$, and $(CH_3NH_3)_2CuCl_2Br_2$ materials show typical absorption spectral properties of copper complexes CuX_4^{2-} in square planar coordination,[25,26] as shown in Figure S2, Supporting Information, compatible with the strong Jahn–Teller distortion observed in the XRD analysis. The corresponding absorption coefficients of the obtained absorption results for the prepared materials have been calculated and plotted, as shown in Figure 4a. Strong bands for each material with absorption coefficients up to 35000 cm^{-1} existed between 300 and 500 nm. Also, the strong bands exemplifying the electronic transitions for $(CH_3NH_3)_2CuCl_2X_2$ can be designed to ligand-to-metal charge-transfer transitions, as mentioned before for $CuCl_4^{2-}$ complexes.[26] Interestingly, band gap energies with weaker and broad bands between 550 and 700 nm contributed to the absorption results. These bands can be explained by the d–d transitions within the d levels of Cu and do not shift for varying C/I/Br content ratio. Also, these bands were in agreement with the sequence of photoluminescence (PL) spectra of the same materials, as shown in Figure 4b. Steady-state PL experiments were performed to estimate the influence of PL quenching of Cu-based perovskite materials. As mentioned in Figure 4b, the

DOI: 10.1021/acsami.8b00495
ACS Appl. Mater. Interfaces 2018, 10, 11699–11707

Table 1. FT-IR Spectral Data for $(CH_3NH_3)_2CuX_4$ Systems

compound	υ(NH-alph)	υ[CH_3-alph (asymm)]	υ[CH_3-alph (symm)]	δ[CH-alph (bending)]		υ(C−N)	υ(Cu−I)	υ(Cu−Br)	υ(Cu−Cl)
$(CH_3NH_3)_2CuCl_4$	3446	2959	2834	1466	1354	964			494
$(CH_3NH_3)_2CuCl_2I_2$	3453	2972	2835	1445	1356	900	543		
$(CH_3NH_3)_2CuCl_2Br_2$	3446	2940	2829	1487	1344	958		559	

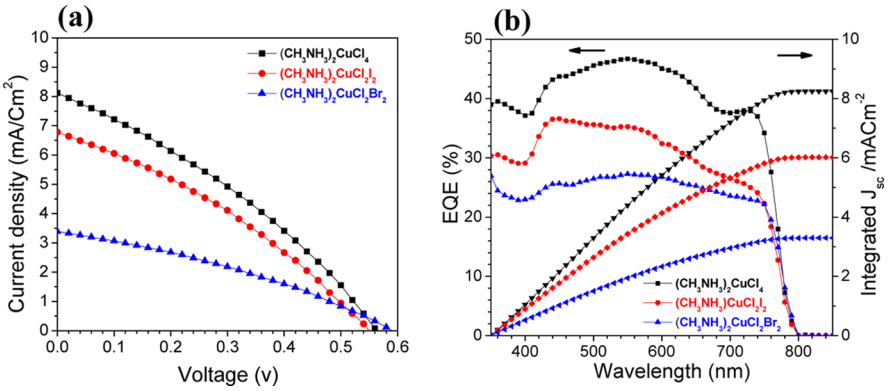

Figure 5. (a) Current−voltage [J−V] curves and (b) EQE spectra of the solar cells consisting of $(CH_3NH_3)_2CuCl_4$ (black color), $(CH_3NH_3)_2CuCl_2I_2$ (red color), and $(CH_3NH_3)_2CuCl_2Br_2$ (blue color) perovskites as absorber materials.

PL intensities of Cu-based perovskite materials decreased in the order of $(CH_3NH_3)_2CuCl_2Br_2$ > $(CH_3NH_3)_2CuCl_2I_2$ > $(CH_3NH_3)_2CuCl_4$ films, indicating the best charge separation and low recombination ability in the reverse order, due to the presence of an efficient nonradiative process to quench the PL effectively. Also, the existence of bromine is essential for the reduction process, as proposed by the PL trend culminating in the stronger emission of $(CH_3NH_3)_2CuCl_2Br_2$, whereas the existence of chlorine ions helps to stabilize the Cu^{2+} oxidation state.[27] The important infrared spectral bands of $(CH_3NH_3)_2CuCl_4$, $(CH_3NH_3)_2CuCl_2I_2$, and $(CH_3NH_3)_2CuCl_2Br_2$ films were examined between 400 and 4000 cm^{-1}. The data are collectively shown in Table 1, and Figure 4c shows the infrared spectra. It can be seen that a broad band was found at 3446−3453 cm^{-1}, which was attributed to −NH of the amine group. Moreover, two strong bands between 2829−2835 and 2940−2972 cm^{-1} were ascribed to the symmetric and asymmetric stretching modes of CH_3. Besides, bending bands between 1344 and 1487 cm^{-1} indicated the −CH of the alkyl group and were consistent with the symmetric bending mode of the NH_3^+ group. The C−N stretching vibration of $CH_3NH_3^+$ appeared at 990−964 cm^{-1}. Furthermore, the strong band observed at 494 cm^{-1} was assigned to the Cu−Cl group, and this band was shifted to 543 cm^{-1} for Cu−I. Finally, bands at 559 cm^{-1} were assigned and confirmed for Cu−Br.[28,29] Besides, UV−vis spectra in the diffuse reflectance mode were used to measure the optical band gap energies using the reflectance data according to the Kubelka−Munk equation.[30,31] Figure 4d predicts the band gap energy values for $(CH_3NH_3)_2CuCl_4$, $(CH_3NH_3)_2CuCl_2I_2$, and $(CH_3NH_3)_2CuCl_2Br_2$, which were found to be 2.36, 1.99, and 1.04 eV, respectively. Furthermore, Figure 3d evinces the change in color for the powders from yellow to dark brown by changing the Cl/I/Br content ratio, which indicates the modulation of their band gap energies.[32−34]

For the simulation study of our systems, models of solar cells were constructed with thin film stacks of glass/FTO/TiO_2/$(CH_3NH_3)_2CuX$/spiro-OMeTAD/Au (where X = Cl_4, Cl_2I_2, and Cl_2Br_2), as shown in Figure S3, Supporting Information. Optimization of the device structure $(CH_3NH_3)_2CuX$ was obtained by different techniques such as PL, structure evaluation, UV−visible absorption, and optical band gap characterization. The electron-transport layer and HTL as parameters for the simulation of the assembled devices are summarized in Table S2, Supporting Information, which were neatly chosen from previously reported experimental works.[36−41] In this context, the three different configuration devices were compared using wxAMPS software, an update of the popular solar cell simulation tool (AMPS; analysis of microelectronic and photonic structures). Also, we represented the three configurations by device-A for $(CH_3NH_3)_2CuCl_4$, device-B for $(CH_3NH_3)_2CuCl_2I_2$, and device-C for $(CH_3NH_3)_2CuCl_2Br_2$, where the active layers were used. Capture cross sections of both electrons and holes were set to 1×10^{-16} cm^2, which results in a carrier diffusion length of ~1 μm in absorber materials. The energy level defects in the simulated thin film materials were located at the center of their band gap with the Gaussian-type energetic distribution (a characteristic energy of 0.1 eV). The tail characteristic energy was 0.01 eV with a band tail density of states of 1×10^{14} cm^{-3}/eV. The bimolecular electron−hole recombination rate has the most significant influence on the performance of the solar cell. Therefore, it was set as 1×10^{-11} cm^3 s^{-1} in the base-line simulation model as reported in the recombination rate ranging from 10^{-11} to 10^{-9} cm^3 s^{-1}.[31] The surface recombination velocities of electrons and holes at the top and bottom electrodes were set to be 1×10^7 cm·s^{-1}. Figure S4a and Table S3, Supporting Information, illustrate the simulated J−V characteristics and summarize the photovoltaic parameters for the cells assembled from different types of active materials, respectively. The simulated device from $CH_3NH_3CuCl_2Br$ delivered the lowest simulated PCE of 15.03%, with an open-circuit voltage (V_{oc}) of 0.845 V, a short-circuit current density (J_{sc}) of 21.78 mA cm^{-2}, and a fill factor (FF) of 81%, whereas $(CH_3NH_3)_2CuCl_4$ displayed the highest conversion efficiency of 21.76% with V_{oc}, J_{sc}, FF of 1.1 V, 23.3 mA cm^{-2}, and 85%, respectively. In addition, the high V_{oc} and low conversion efficiency of $(CH_3NH_3)_2CuCl_2Br_2$ were assigned to the narrow

DOI: 10.1021/acsami.8b00495
ACS Appl. Mater. Interfaces 2018, 10, 11699−11707

spectral response with a band gap of about 1.04 eV. It is clear that the simulated results here should supply the insight, grasp the function of each part in solar cells, and help to set device parameters that permit for further analysis and design optimization. The external quantum efficiency (EQE) spectra for the corresponding cells are revealed in Figure S4b, Supporting Information. $(CH_3NH_3)_2CuCl_4$ shows an improvement in the wavelength between 200 and 840 nm with the highest intensity above 90%, and an intensity below 90% for $(CH_3NH_3)_2CuCl_2I_2$ was revealed, whereas the $(CH_3NH_3)_2CuCl_2Br_2$ cell depicted about 80% with a wavelength range from 380 to 810 nm. Besides that, $J-V$ characteristics as well as the corresponding spectra of the EQE for our cells using different perovskite materials were experimentally studied, as shown in Figure 5a,b, respectively. Perovskite materials $(CH_3NH_3)_2CuX$ (X = Cl_4, Cl_2I_2, and Cl_2Br_2) were sensitized by light, and the photocurrent measurements were performed (Figure 5a). The obtained results indicated that $(CH_3NH_3)_2CuCl_4$ yielded a PCE of 2.41%, with J_{sc} = 8.12 mA/cm^2, V_{oc} = 0.560 V, and FF = 0.52, whereas they were η = 1.75%, J_{sc} = 6.78 mA/cm^2, V_{oc} = 0.545 V, and FF = 0.47 and η = 0.99%, J_{sc} = 3.35 mA/cm^2, V_{oc} = 0.581 V, and FF = 0.50 for $(CH_3NH_3)_2CuCl_2I_2$ and $(CH_3NH_3)_2CuCl_2Br_2$, respectively. $(CH_3NH_3)_2CuCl_2Br_2$ gave a much lower PCE despite the optimized band gap. Cu^{2+} reduction caused by the higher trap density can explain the lower performance of $(CH_3NH_3)_2CuCl_2Br_2$.[42] Furthermore, Table 2 summarizes the obtained photocurrent characteristic parameters for the three different cells assembled using the three different perovskite materials. Moreover, a small effect of hysteresis was observed for all devices using the three different structures of perovskite materials, as shown in Figure S5, Supporting Information. One can notice that the cell conversion efficiency as well as the hysteretic behavior was affected by the scan range with varied initial bias.[43] It is clearly observed that the difference in the cell performance between forward and reverse scans comes from bias start direction. The forward one can degrade the performance because it starts with a negative bias, whereas the performance can be enhanced in the case of the reverse scan because it starts with a positive bias.[44] Although a low conversion efficiency was obtained for the devices under investigation in this study, we obtained a low hysteresis effect, which may be come from the existence of transition metal (copper).[45] The acquired results were expected to come from the fact that a given voltage-settling interval is too short to distinguish the small difference in capacitive current.[46]

Table 2. $I-V$ Characteristics of the Copper-Based Lead-Free, PSCs Manufactured Using$(CH_3NH_3)_2CuCl_4$, $(CH_3NH_3)_2CuCl_2I_2$, and $(CH_3NH_3)_2CuCl_2Br_2$ Cells Measured with Standard AM 1.5G (100 mW/cm^2)

samples	J_{SC}/mA cm^{-2}	V_{OC}/V	FF	η/%
$(CH_3NH_3)_2CuCl_4$	8.12	0.560	52.99	2.41
$(CH_3NH_3)_2CuCl_2I_2$	6.78	0.545	47.41	1.75
$(CH_3NH_3)_2CuCl_2Br_2$	3.35	0.581	50.86	0.99

From the theoretical calculations (Table S1, Supporting Information) and the previous related studies,[17] the valence bands (VBs) of $(CH_3NH_3)_2CuCl_4$ and $(CH_3NH_3)_2CuCl_2I_2$ of −5.84 and −5.61 eV, respectively, were in a good agreement with the HOMO level of spiro-OMeTAD HTL (−5.2 eV), whereas the VB of $(CH_3NH_3)_2CuCl_2Br_2$ was −4.98 eV, which revealed a mismatch with the HOMO of spiro-OMeTAD (−5.2 eV),[47] suggesting poor hole transfer in the device. The reason behind the low efficiency obtained in all used perovskite materials for our cells may come from the recombination occurred in the cells. Also, the EQE spectra in Figure 5b show a maximum value of ∼45% in the wavelength range between 400 and 800 nm, which is in agreement with the best photocurrent obtained for the devices. Figure 5b also shows the EQE integration results over the AM1.5 solar spectrum at an irradiance of 100 mW cm^{-2}, which give J_{sc} values of 8.25, 6.02, and 3.29 mA cm^{-2} for different copper perovskite devices of $(CH_3NH_3)_2CuCl_4$, $(CH_3NH_3)_2CuCl_2I_2$, and $(CH_3NH_3)_2CuCl_2Br_2$, respectively. J_{sc} was measured to be 8.12, 6.78, and 3.35 mA cm^{-2}, respectively, for the studied cells. The experimental uncertainties can explain the differences between the currents estimated from the EQE integration and the $J-V$ measurements. It is worth noting that the cells were tested in air without further encapsulation; there is usually a little bit degraded performance for these PSCs following testing.[48] By comparing our efficiency results with those of the other researchers who used copper green perovskite materials, we found that the structure of the cells designed has an important role in controlling the estimated net efficiency obtained.[49] In the case of cortecchia et al.,[17] they used a planar structure, whereas in our work, we used a mesoporous structure for PSCs. Charge diffusion, good homogeneity, and thicknesses of the films are important factors for good cell efficiency; trade-off between these factors causes poor photovoltaic efficiency. Planar-structured solar cells can confirm this phenomenon, where the charge transport cannot traverse the layers because of the preferential orientation of the perovskite toward the heavy hole and electron effective masses for transport in reciprocal space. Therefore, to solve this problem, using a mesoporous TiO_2 layer is essential; it permits the disarrangement of the continuous 2D perovskite structure, enhancing the charge extraction from the material as well as the vertical charge transport in the device. Besides the advantages of using mesoporous structures for improving the charge extraction, some disadvantages of these structures appear plainly for the homogeneity of the perovskite materials after the deposition above the TiO_2 mesoporous layer. The results obtained from FE-SEM show that the homogeneity of perovskite layers on TiO_2 mesoporous is not good, which is undoubtedly considered to be one of the reasons behind the low net conversion efficiency of the assembled cells, as also noticed from the $J-V$ characteristics results. Additionally, the low efficiency achieved for copper-based PSCs may come from the formation of Cu^+ trap states during the film formation, but the good thing behind using copper-based lead-free perovskite devices is the efficient luminescence coming from in situ formed Cu^+ ions.

CONCLUSIONS

We discussed the synthesis of copper (Cu)-based hybrid perovskite materials, with the general formula of $(CH_3NH_3)_2CuX$ (X = Cl_4, Cl_2I_2, and Cl_2Br_2) for environment-friendly PSCs. We studied copper metal as a suitable substitutional element to change the lead in metal halide perovskites and the functionality from experimental and theoretical view. Stability and toxicity issues in PSCs can be solved using organocopper-based perovskite materials, which have different advantages such as ambient stability and ease of processing with wet chemical solution methods with low-

DOI: 10.1021/acsami.8b00495
ACS Appl. Mater. Interfaces 2018, 10, 11699−11707

temperature preparation. The essential role of Cl^- for stabilization of the devices was studied. $J-V$ characteristics as well as the corresponding spectra of the EQE for our cells using different perovskite materials were experimentally studied and estimated theoretically. The obtained results indicated that $(CH_3NH_3)_2CuCl_4$ yielded a PCE (η) of 2.41%, whereas they were 1.75% and 0.99% for $(CH_3NH_3)_2CuCl_2I_2$ and $(CH_3NH_3)_2CuCl_2Br_2$, respectively. $(CH_3NH_3)_2CuCl_2Br_2$ gave a much lower PCE despite the optimized band gap. Cu^{2+} reduction caused by the higher trap density can explain the lower performance of $(CH_3NH_3)_2CuCl_2Br_2$.

EXPERIMENTAL METHODS

Materials. Hydroiodic acid (HI) (57 wt % in water), hydrobromic acid (HBr) (aqueous solution 48 wt %), hydrochloric acid (HCl) (aqueous solution 35 wt %), methyl amine (CH_3NH_2), and copper chloride ($CuCl_2$) were bought from Alfa Aesar and used as the starting materials for the synthesis of $(CH_3NH_3)_2CuX$ (X = Cl_4, Cl_2I_2, and Cl_2Br_2) using a grinding milling pathway.

Preparation of (CH_3NH_2-X) (X = Cl, I, and Br). Commonly, methyl amine CH_3NH_2 solution (21.6 mL, 40 mass % in water, Alfa Aesar) was reacted with equimolar hydrochloric acid (HCl) or hydroiodic acid (HI) or hydrobromic acid (HBr) (30 mL, with hypophosphorous acid 1.5%, Alfa Aesar) and kept stirred at 0 °C for 2 h under a N_2 atmosphere, to synthesize methyl ammonium halide CH_3NH_3Cl, CH_3NH_3I, or CH_3NH_3Br, respectively. After that, CH_3NH_3X was crystallized using a rotary evaporator at 80 °C for 2 h to remove the solvent, then washed three times with diethyl ether (99%, anhydrous, ECHO), and dried in a vacuum oven at 50 °C overnight before use.

Synthesis of $(CH_3NH_3)_2CuCl_2X_2$ (X = Cl, I, and Br) Perovskite Precursor Solution. One mole (507 mg) of $CuCl_2$ powder was manually ground with 2 mol (350 mg) of (CH_3NH_3Cl) or (CH_3NH_3I) or (CH_3NH_3Br) powders in an agate mortar for 10 min to produce $(CH_3NH_3)_2CuCl_4$, $(CH_3NH_3)_2CuCl_2I_2$, and $(CH_3NH_3)_2CuCl_2Br_2$ compositions, respectively. After that, the obtained ground powders were dissolved in 1 mL of *N*,*N*-dimethyl formamide (anhydrous, Aldrich). The solution was stirred at 70 °C for 1 h and filtered to be ready to use.

Device Assembling Process. The electrodes as well as the devices were fabricated, as described elsewhere.[38,50] All device fabrication steps are the same as our previous published work;[2,38] the only difference in this work is using the prepared $(CH_3NH_3)_2CuX_4$ [$(CH_3NH_3)_2CuCl_4$ or $(CH_3NH_3)_2CuCl_2I_2$ or $(CH_3NH_3)_2CuCl_2Br_2$] precursor solution as a perovskite sensitizer.

Characterization and Material Testing. A Bruker D8-ADVANCE machine was used for XRD patterns to detect the obtained materials. An FE-SEM model (JSM-5400, JEOL instrument, Japan) and an atomic force microscope (Nanosurf C300 Controller Flex AFM, Switzerland) were used to obtain the micrographs of the studied samples. A UV−vis−NIR spectrophotometer (JASCO-V-570 spectrophotometer, Japan) detects the UV−vis absorption and diffuse reflectance spectrum. Furthermore, PL spectra were checked with a fluorescence spectrophotometer (Shimadzu RF-5301PC, Kyoto, Japan). In addition, the Fourier transform infrared (FT-IR) absorption spectrum was obtained using a JASCO 3600 spectrophotometer. A solar simulator (Solar Light Co. Inc.) with a Keithley 2420 source was used to characterize the device performance. The calibration of the simulator-integrated light was performed using a certified silicon reference cell. Furthermore, a measurement system (PVE 300, Bentham) that comprised a xenon lamp, a monochromator, a chopper, a lock-in amplifier, and a calibrated silicon photodetector was employed to permit the quick and accurate determination of external quantum efficiency (EQE/IPCE).

Theoretical Simulation Methods. wxAMPS simulation program software was adjusted for the theoretical study and device modeling to simulate electron transport of our assembled cells based on copper perovskite materials.[35]

ASSOCIATED CONTENT

Supporting Information

The Supporting Information is available free of charge on the ACS Publications website at DOI: 10.1021/acsami.8b00495.

FESEM micrographs as well as absorption spectra results of $(CH_3NH_3)_2CuCl_4$, $(CH_3NH_3)_2CuCl_2I_2$, and $(CH_3NH_3)_2CuCl_2Br_2$ perovskite films deposited on [TiO_2-meso/FTO] substrate; schematic diagram of simulated PSCs; simulated $J-V$ and EQE curves of $(CH_3NH_3)_2CuCl_4$, $(CH_3NH_3)_2CuCl_2I_2$, and $(CH_3NH_3)_2CuCl_2Br_2$ perovskite materials; and tables summarizing the corresponding simulated photovoltaic parameters, theoretical parameters for copper-based perovskite materials, and basic parameters of the materials used in this study. Furthermore, studing the hysteresis effect showing the reverse and forward scan obtained for the cells used in this study (PDF)

AUTHOR INFORMATION

Corresponding Authors

*E-mail: amourtada@ncepu.edu.cn (A.M.E.).
*E-mail: a.shalan133@gmail.com (A.E.S.).

ORCID

Ahmed Mourtada Elseman: 0000-0001-9297-9866
Ahmed Esmail Shalan: 0000-0002-3424-1609
Meicheng Li: 0000-0002-9756-742X

Author Contributions

‖A.M.E. and A.E.S. equally contributed to this work by pursuing the experimental work as well as writing the manuscript.

Notes

The authors declare no competing financial interest.

ACKNOWLEDGMENTS

Science & Technology Development Fund in Egypt (STDF) as well as CMRDI, Egypt, are appreciated by the authors for their assistance to follow up this study through project grant no. 25250. Furthermore, the technical service unit of CMRDI is also gratefully acknowledged.

REFERENCES

(1) Kojima, A.; Teshima, K.; Shirai, Y.; Miyasaka, T. Organo Metal Halide Perovskites as Visible-Light Sensitizer for Photovoltaic Cells. *J. Am. Chem. Soc.* **2009**, *131*, 6050−6051.

(2) Shalan, A. E.; Narra, S.; Oshikiri, T.; Ueno, K.; Shi, X.; Wu, H.-P.; Elshanawany, M. M.; Diau, E. W.-G.; Misawa, H. Optimization of a Compact Layer of TiO_2 via Atomic-Layer Deposition for High-Performance Perovskite Solar Cells. *Sustainable Energy Fuels* **2017**, *1*, 1533−1540.

(3) Green, M. A.; Emery, K.; Hishikawa, Y.; Warta, W.; Dunlop, E. D. Solar Cell Efficiency Tables (Version 48). *Prog. Photovoltaics* **2016**, *24*, 905−913.

(4) Saliba, M.; Matsui, T.; Domanski, K.; Seo, J.-Y.; Ummadisingu, A.; Zakeeruddin, S. M.; Correa-Baena, J.-P.; Tress, W. R.; Abate, A.; Hagfeldt, A.; Gratzel, M. Incorporation of Rubidium Cations into Perovskite Solar Cells Improves Photovoltaic Performance. *Science* **2016**, *354*, 206−209.

(5) Stoumpos, C. C.; Kanatzidis, M. G. The Renaissance of Halide Perovskites and Their Evolution as Emerging Semiconductors. *Acc. Chem. Res.* **2015**, *48*, 2791−2802.

(6) Grätzel, M. The Light and Shade of Perovskite Solar Cells. *Nat. Mater.* **2014**, *13*, 838−842.

(7) Brenner, T. M.; Egger, D. A.; Kronik, L.; Hodes, G.; Cahen, D. Hybrid Organic−Inorganic Perovskites: Low-Cost Semiconductors

DOI: 10.1021/acsami.8b00495
ACS Appl. Mater. Interfaces 2018, 10, 11699−11707

with Intriguing Charge-Transport Properties. *Nat. Rev. Mater.* **2016**, *1*, 15007.
(8) Bashouti, M. Y.; Resch, S.; Ristein, J.; Mačković, M.; Spiecker, E.; Waldvogel, S. R.; Christiansen, S. H. Functionalization of Silver Nanowires Surface using Ag-C Bonds in a Sequential Reductive Method. *ACS Appl. Mater. Interfaces* **2015**, *7*, 21657−21661.
(9) Bashouti, M. Y.; Pietsch, M.; Brönstrup, G.; Sivakov, V.; Ristein, J.; Christiansen, S. Heterojunction based hybrid silicon nanowire solar cell: surface termination, photoelectron and photoemission spectroscopy study. *Prog. Photovoltaics* **2014**, *22*, 1050−1061.
(10) Liu, J.; Gao, C.; Luo, L.; Ye, Q.; He, X.; Ouyang, L.; Guo, X.; Zhuang, D.; Liao, C.; Mei, J.; Lau, W. Low-Temperature, Solution Processed Metal Sulfide as an Electron Transport Layer for Efficient Planar Perovskite Solar Cells. *J. Mater. Chem. A* **2015**, *3*, 11750−11755.
(11) Liu, J.; Wang, G.; Song, Z.; He, X.; Luo, K.; Ye, Q.; Liao, C.; Mei, J. $FAPb_{1-x}Sn_xI_3$ Mixed Metal Halide Perovskites with Improved Light Harvesting and Stability for Efficient Planar Heterojunction Solar Cells. *J. Mater. Chem. A* **2017**, *5*, 9097−9106.
(12) Giustino, F.; Snaith, H. J. Toward Lead-Free Perovskite Solar Cells. *ACS Energy Lett.* **2016**, *1*, 1233−1240.
(13) Yu, Y.; Zhao, D.; Grice, C. R.; Meng, W.; Wang, C.; Liao, W.; Cimaroli, A. J.; Zhang, H.; Zhu, K.; Yan, Y. Thermally Evaporated Methylammonium Tin Triiodide Thin Films for Lead-Free Perovskite Solar Cell Fabrication. *RSC Adv.* **2016**, *6*, 90248−90254.
(14) Bashouti, M. Y.; Yousefi, P.; Ristein, J.; Christiansen, S. H. Electronic Properties of Si−Hx Vibrational Modes at Si Waveguide Interface. *J. Phys. Chem. Lett.* **2015**, *6*, 3988−3993.
(15) Singh, T.; Kulkarni, A.; Ikegami, M.; Miyasaka, T. Effect of Electron Transporting Layer on Bismuth-Based Lead-Free Perovskite $(CH_3NH_3)_3$ Bi_2I_9 for Photovoltaic Applications. *ACS Appl. Mater. Interfaces* **2016**, *8*, 14542−14547.
(16) Jiang, F.; Yang, D.; Jiang, Y.; Liu, T.; Zhao, X.; Ming, Y.; Luo, B.; Qin, F.; Fan, J.; Han, H.; Zhang, L.; Zhou, Y. Chlorine-Incorporation-Induced Formation of the Layered Phase for Antimony-Based Lead-Free Perovskite Solar Cells. *J. Am. Chem. Soc.* **2018**, *140*, 1019−1027.
(17) Cortecchia, D.; Dewi, H. A.; Yin, J.; Bruno, A.; Chen, S.; Baikie, T.; Boix, P. P.; Grätzel, M.; Mhaisalkar, S.; Soci, C.; Mathews, N. Lead-Free $MA_2CuCl_xBr_{4-x}$ Hybrid Perovskites. *Inorg. Chem.* **2016**, *55*, 1044−1052.
(18) Im, J.-H.; Chung, J.; Kim, S.-J.; Park, N.-G. Synthesis, Structure, and Photovoltaic Property of a Nanocrystalline 2H Perovskite-Type Novel Sensitizer $(CH_3CH_2NH_3)PbI_3$. *Nanoscale Res. Lett.* **2012**, *7*, 353.
(19) Khan, N. A.; Jhung, S. H. Remarkable Adsorption Capacity of $CuCl_2$ Loaded Porous Vanadium Benzene Dicarboxylate for Benzothiophene. *Angew. Chem.* **2012**, *124*, 1224−1227.
(20) Saraireh, S. A.; Altarawneh, M. Electronic Structure of the $CuCl_2$ (100) Surface: A DFT First-Principle Study. *J. Nanomater.* **2012**, *2012*, 767128.
(21) Heo, J. H.; Im, S. H. Highly Reproducible, Efficient Hysteresis-Less $CH_3NH_3PbI_{3-x}Cl_x$ Planar Hybrid Solar Cells without Requiring Heat-Treatment. *Nanoscale* **2016**, *8*, 2554−2560.
(22) Park, N.-G. Perovskite Solar Cells: An Emerging Photovoltaic Technology. *Mater. Today* **2015**, *18*, 65−72.
(23) Tavakoli, M. M.; Gu, L.; Gao, Y.; Reckmeier, C.; He, J.; Rogach, A. L.; Yao, Y..; Fan, Z. Fabrication of Efficient Planar Perovskite Solar Cells Using a One-Step Chemical Vapor Deposition Method. *Sci. Rep.* **2015**, *5*, 14083.
(24) Shalan, A. E.; Oshikiri, T.; Sawayanagi, H.; Nakamura, K.; Ueno, K.; Sun, Q.; Wu, H.-P.; Diau, E. W.-G.; Misawa, H. Versatile Plasmonic-Effects at The Interface of Inverted Perovskite Solar Cells. *Nanoscale* **2017**, *9*, 1229−1236.
(25) Basolo, F. Substitution Reactions of Square Planar Complexes. *Advances in Chemistry*; ACS Publications, 1965; Vol. *49*, Chapter 4, pp 81−106.
(26) Cattalini, L.; Tobe, M. L. Nucleophilic Substitution in Square-Planar Gold (III) Complexes. *Coord. Chem. Rev.* **1966**, *1*, 106−110.
(27) Jayawardena, K. D. G. I.; Rozanski, L. J.; Mills, C. A.; Beliatis, M. J.; Nismy, N. A.; Silva, S. R. P. Inorganics-in-Organics: Recent Developments and Outlook for 4G Polymer Solar Cells. *Nanoscale* **2013**, *5*, 8411−8427.
(28) Mosconi, E.; Quarti, C.; Ivanovska, T.; Ruani, G.; De Angelis, F. Structural and Electronic Properties of Organo-Halide Lead Perovskites: A Combined IR-Spectroscopy and ab Initio Molecular Dynamics Investigation. *Phys. Chem. Chem. Phys.* **2014**, *16*, 16137−16144.
(29) Pérez-Osorio, M. A.; Milot, R. L.; Filip, M. R.; Patel, J. B.; Herz, L. M.; Johnston, M. B.; Giustino, F. Vibrational Properties of The Organic−Inorganic Halide Perovskite CH3NH3PbI3 from Theory and Experiment: Factor Group Analysis, First-Principles Calculations, and Low-Temperature Infrared Spectra. *J. Phys. Chem. C* **2015**, *119*, 25703−25718.
(30) Kubelka, V. P. Ein Beintrag zur Optik der Farbanstriche. *Z. Tech. Phys.* **1931**, *12*, 593−601.
(31) Elseman, A. M.; Rashad, M. M.; Hassan, A. M. Easily Attainable, Efficient Solar Cell with Mass Yield of Nanorod Single-Crystalline Organo-Metal Halide Perovskite Based on a Ball Milling Technique. *ACS Sustainable Chem. Eng.* **2016**, *4*, 4875−4886.
(32) Colella, S.; Mosconi, E.; Fedeli, P.; Listorti, A.; Gazza, F.; Orlandi, F.; Ferro, P.; Besagni, T.; Rizzo, A.; Calestani, G.; Gigli, G.; De Angelis, F.; Mosca, R. $MAPbI_{3-x}Cl_x$ Mixed Halide Perovskite for Hybrid Solar Cells: The Role of Chloride as Dopant on the Transport and Structural Properties. *Chem. Mater.* **2013**, *25*, 4613−4618.
(33) Rashad, M. M.; Hassan, A. M.; Nassar, A. M.; Ibrahim, N. M.; Mourtada, A. A New Nano-Structured Ni (II) Schiff Base Complex: Synthesis, Characterization, Optical Band Gaps, and Biological Activity. *Appl. Phys. A: Mater. Sci. Process.* **2014**, *117*, 877−890.
(34) Edri, E.; Kirmayer, S.; Kulbak, M.; Hodes, G.; Cahen, D. Chloride Inclusion and Hole Transport Material Doping to Improve Methyl Ammonium Lead Bromide Perovskite-Based High Open-Circuit Voltage Solar Cells. *J. Phys. Chem. Lett.* **2014**, *5*, 429−433.
(35) Elseman, A. M.; Shalan, A. E.; Rashad, M. M.; Hassan, A. M. Experimental and Simulation Study for Impact of Different Halides on The Performance of Planar Perovskite Solar Cells. *Mater. Sci. Semicond. Process.* **2017**, *66*, 176−185.
(36) Wang, Y.; Xia, Z.; Liu, Y.; Zhou, H. Simulation of Perovskite Solar Cells with Inorganic Hole Transporting Materials. *Photovoltaic Specialist Conference (PVSC), IEEE*, 42nd; IEEE, 2015; pp 1−4.
(37) Cuiffi, J.; Benanti, T.; Nam, W. J.; Fonash, S. Modeling of Bulk and Bilayer Organic Heterojunction Solar Cells. *Appl. Phys. Lett.* **2010**, *96*, 143307.
(38) Shalan, A. E.; Oshikiri, T.; Narra, S.; Elshanawany, M. M.; Ueno, K.; Wu, H.-P.; Nakamura, K.; Shi, X.; Diau, E. W.-G.; Misawa, H. Cobalt Oxide (CoO_x) as an Efficient Hole-Extracting Layer for High-Performance Inverted Planar Perovskite Solar Cells. *ACS Appl. Mater. Interfaces* **2016**, *8*, 33592−33600.
(39) Wang, T.; Chen, J.; Wu, G.; Song, D.; Li, M. Designing Novel Thin Film Polycrystalline Solar Cells for High Efficiency: Sandwich CIGS and Heterojunction Perovskite. *J. Semicond.* **2017**, *38*, 014005.
(40) Wang, T.; Chen, J.; Wu, G.; Li, M. Optimal Design of Efficient Hole Transporting Layer Free Planar Perovskite Solar Cell. *Sci. China Mater.* **2016**, *59*, 703−709.
(41) Liu, F.; Zhu, J.; Wei, J.; Li, Y.; Lv, M.; Yang, S.; Zhang, B.; Yao, J.; Dai, S. Numerical Simulation: Toward the Design of High-Efficiency Planar Perovskite Solar Cells. *Appl. Phys. Lett.* **2014**, *104*, 253508.
(42) Sheng, R.; Ho-Baillie, A.; Huang, S.; Chen, S.; Wen, X.; Hao, X.; Green, M. A. Methylammonium Lead Bromide Perovskite-Based Solar Cells by Vapor-Assisted Deposition. *J. Phys. Chem. C* **2015**, *119*, 3545−3549.
(43) Wei, J.; Zhao, Y.; Li, H.; Li, G.; Pan, J.; Xu, D.; Zhao, Q.; Yu, D. Hysteresis Analysis Based on the Ferroelectric Effect in Hybrid Perovskite Solar Cells. *J. Phys. Chem. Lett.* **2014**, *5*, 3937−3945.
(44) Chen, B.; Zheng, X.; Yang, M.; Zhou, Y.; Kundu, S.; Shi, J.; Zhu, K.; Priya, S. Interface band structure engineering by ferroelectric polarization in perovskite solar cells. *Nano Energy* **2015**, *13*, 582−591.

DOI: 10.1021/acsami.8b00495
ACS Appl. Mater. Interfaces 2018, 10, 11699−11707

(45) Tang, Z.; Bessho, T.; Awai, F.; Kinoshita, T.; Maitani, M. M.; Jono, R.; Murakami, T. N.; Wang, H.; Kubo, T.; Uchida, S.; Segawa, H. Hysteresis-free perovskite solar cells made of potassium-doped organometal halide perovskite. *Sci. Rep.* **2017**, *7*, 12183.
(46) Chen, B.; Yang, M.; Priya, S.; Zhu, K. Origin of J−V Hysteresis in Perovskite Solar Cells. *J. Phys. Chem. Lett.* **2016**, *7*, 905−917.
(47) Kang, T.; Tsai, C.-M.; Jiang, Y.-H.; Gollavelli, G.; Mohanta, N.; Diau, E. W.-G.; Hsu, C.-S. Interfacial Engineering with Cross-Linkable Fullerene Derivatives for High-Performance Perovskite Solar Cells. *ACS Appl. Mater. Interfaces* **2017**, *9*, 38530−38536.
(48) Tsai, C.-M.; Mohanta, N.; Wang, C.-Y.; Lin, Y.-P.; Yang, Y.-W.; Wang, C. L.; Hung, C.-H.; Diau, E. W.-G. Formation of Stable Tin Perovskites Co-crystallized with Three Halides for Carbon-Based Mesoscopic Lead-Free Perovskite Solar Cell. *Angew. Chem., Int. Ed.* **2017**, *56*, 13819−13823.
(49) Salim, T.; Sun, S.; Abe, Y.; Krishna, A.; Grimsdale, A. C.; Lam, Y. M. Perovskite-Based Solar Cells: Impact of Morphology and Device Architecture on Device Performance. *J. Mater. Chem. A* **2015**, *3*, 8943−8969.
(50) Chung, C.-C.; Lee, C. S.; Jokar, E.; Kim, J. H.; Diau, E. W.-G. Well-Organized Mesoporous TiO_2 Photoanode by Using Amphiphilic Graft Copolymer for Efficient Perovskite Solar Cells. *J. Phys. Chem. C* **2016**, *120*, 9619−9627.

DOI: 10.1021/acsami.8b00495
ACS Appl. Mater. Interfaces 2018, 10, 11699−11707